HHS Public Access

Author manuscript

Robotica. Author manuscript; available in PMC 2023 November 17.

Published in final edited form as:

Robotica. 2023 May ; 41(5): 1536–1549. doi:10.1017/s0263574722001862.

Theoretical error analysis of spotlight-based instrument localization for retinal surgery

Mingchuan Zhou[1,*], **Felix Hennerkes**[2], **Jingsong Liu**[2], **Zhongliang Jiang**[2], **Thomas Wendler**[2], **M. Ali Nasseri**[3], **Iulian Iordachita**[4], **Nassir Navab**[2]

[1]College of Biosystems Engineering and Food Science, Zhejiang University, Hangzhou, China,

[2]Chair for Computer Aided Medical Procedures and Augmented Reality, Computer Science Department, Technische Universität München, Munchen, Germany,

[3]Augenklinik und Poliklinik, Klinikum rechts der Isar der Technische Universität München, München, Germany,

[4]Department of Mechanical Engineering and Laboratory for Computational Sensing and Robotics, Johns Hopkins University, Baltimore, MD, USA

Abstract

Retinal surgery is widely considered to be a complicated and challenging task even for specialists. Image-guided robot-assisted intervention is among the novel and promising solutions that may enhance human capabilities therein. In this paper, we demonstrate the possibility of using spotlights for 5D guidance of a microsurgical instrument. The theoretical basis of the localization for the instrument based on the projection of a single spotlight is analyzed to deduce the position and orientation of the spotlight source. The usage of multiple spotlights is also proposed to check the possibility of further improvements for the performance boundaries. The proposed method is verified within a high-fidelity simulation environment using the 3D creation suite Blender. Experimental results show that the average positioning error is 0.029 mm using a single spotlight and 0.025 mm with three spotlights, respectively, while the rotational errors are 0.124 and 0.101, which shows the application to be promising in instrument localization for retinal surgery.

Keywords

retinal surgery; image-guided surgery; needle pose estimation

1. Introduction

In 2019, more than 342 million patients were identified as having retinal diseases, and a significant number of these required a microsurgical intervention in order to preserve or

[*]Corresponding author. mczhou@zju.edu.cn.

Authors' contributions. Mingchuan Zhou: Conceptualization, investigation, methodology, modeling, design, simulation, writing, funding. Felix Hennerkes: Methodology, modeling, writing. Jingsong Liu: Investigation, methodology. Zhongliang Jiang: Methodology, Writing, revising. Thomas Wendler and M. Ali Nasseri: Methodology, editing. Iulian Iordachita: Methodology, modeling, writing, and funding. Nassir Navab: Methodology, modeling, writing, revising, and funding.

Conflicts of interest. The authors declare none.

restore vision [1]. However, retinal surgery is characterized by a complex workflow and delicate tissue manipulations that require both critical manual dexterity and learned surgical skills [2]. Many of these patients lack access to proper and timely treatment and therefore increase their chances of blindness. Medical robots and robot-assisted surgery (RAS) setups are envisioned as a potential solution for reducing the work intensity, improving the surgical outcomes, and extending the work lifetime of experienced surgeons [3–14]. Different from the robotic laparoscopic minimally invasive surgery, the retinal surgery needs further consideration of specific precision which requires additional design in robotic system [14, 15]. In 2016, surgeons at Oxford's John Radcliffe Hospital performed the world's first robot-assisted eye surgery, demonstrating the safety and the possibility of using a robot system in the most challenging task in retinal surgery [16], namely the dissection of the epiretinal or inner limiting membrane over the macula.

Autonomous technology has been first proposed by David L. Heiserman in 1976 [17] and has been developed rapidly because of large-scale research and business attempts in autonomous driving (AD) [18]. Not only restricted to applications in AD, but the introduction of autonomy into RAS may also someday assist microsurgeons to perform surgery with better outcomes and higher efficiency [9, 19–23].

A proper sensing method for instrument localization is fundamental for autonomous tasks in retinal surgery. Zhou et al. [24] utilized microscope-integrated optical coherence tomography (MI-OCT) to perform subretinal insertion under visual servoing. However, MI-OCT has a very limited visual depth of roughly 2 mm. Hence, it is hard for it to meet the requirements for some tasks with large-scale navigation inside the eye. The boundaries constraining the instruments' movement range depend on the applications and could be treated as a volume of 10 mm × 10 mm × 5 mm [25, 26]. This estimation is based on the available microscope view for some typical retinal surgeries, that is navigating needles close to the retina or tracking vessel.

The contradiction of the image resolution and image range of OCT makes it less suitable for the guidance of instrument movements over a large range, for example a volume of 10 mm × 10 mm × 5 mm. To navigate intraocular instruments in 3D with a large range, Probst et al. proposed a stereo-microscope vision system with deep learning to localize the needle tip [26]. This method showed advantages in the simplified in terms of logistics; however, there are constraints due to the need of data annotation and illumination. To cope for this, Yang et al. [27] and Zhou et al. [25] proposed a proactive of method using a spotlight source. Different from Yang et al. [27], spotlight source proposed in this paper is a single spotlight source with a single projection pattern or triple projection pattern which can be mounted on the tooltip. However, the theoretical error analysis and proper guidance for designing a spotlight have not been fully studied and discussed yet.

In this paper, we investigate the theoretical error analysis for spotlight-based instrument localization in 5D for retinal surgery. The error limitations are explored by a sensitivity analysis of the spotlight configuration. The contributions of this paper are listed as follows,

- The detailed mathematical models to derive the pose and position of instrument from a single spotlight and three spotlight are proposed and verified.

- The high-fidelity simulation environment built with Blender [28] shown in Fig. 1 makes it possible to verify the theory under controlled various conditions.
- The experiment results indicate that the single spotlight version can localize the position of the instrument with an average error of 0.028 mm while the multiple spotlights version yields 0.024 mm showing the promising for retinal surgery.

The remainder of the paper is organized as follows: in the next section, we briefly present the related work. The proposed method is described in Section 3. In Section 4, the performance of the proposed method is evaluated and discussed. Finally, Section 5 concludes this paper.

2. Related work

To navigate instruments inside the eye, three approaches have been proposed. The first approach uses the optical coherence tomography (OCT) modality in form of MI-OCT. OCT imaging is popular not only in the retina diagnostics but also intraoperatively to provide useful visual feedback to the operating surgeon [29–32], having the benefits of a suitable resolution and a radiationless imaging mechanism. An additional benefit is that it allows to see the interaction between the tissue and the instrument [33]. However, the image range in depth direction is limited to roughly 2 mm which makes it only suitable for very fine positioning [29], for example internal limiting membrane peeling [34] and subretinal injection [24].

The second approach is stereo-microscope vision. Probst et al. proposed [26] a stereo-microscope vision system which uses deep learning to reconstruct the retina surface and localize the needle tip. The benefit of this method is that it will not introduce any other additional instruments inside the eye. Moreover, the method can obtain an accuracy of 0.1 mm in 3D over a large range (the imaging range of the microscope). The drawback is that the deep learning method requires a large amount of annotated data for different surgical tools and the purely passive stereo-microscope vision systems could be influenced by variations in illumination.

A third is the use of a single microscope to navigate instruments. As the solo microscope image cannot provide the depth information, a structured light-based method can be applied. In this approach, the use of geometrical information is required. The use of light cones and their respective elliptical projections is a commonly selected approach. Chen et al. [35] used the ellipse shape to estimate the extrinsic parameters and the focal length of a camera by using only one single image of two coplanar circles with arbitrary radius. The relationship was also explored by Noo et al. [36] for the calibration of a cone-beam scanner used in both X-ray computed tomography and single-photon emission computed tomography. Swirski et al. [37] used the ellipse shape to estimate the eyeball rotation with the pupil ellipse geometry with a single camera. In the eye surgery domain, Yang et al. [27] used a cone beam with structured light reconstruction to estimate a surface in the coordinate system of a custom-built optical tracking system named ASAP. There, after surface reconstruction, the tip-to-surface distance was estimated in the coordinate system of the ASAP [38]. Inspired by Yang et al.’s approach, Zhou et al. [25] proposed a spotlight to navigate an instrument and

measure the distance between the instrument tip and the surface with real-time performance in a large range of 10 mm × 10 mm × 5 mm.

To further study the spotlight navigation capabilities, in this paper we explore the performance upper limitation with a theoretical analysis. To verify the correctness of the analysis, a high-fidelity simulation environment with Blender is built up and tested with different simulated trajectories. Furthermore, the multi-spotlight design is also analyzed and verified to have the potential to improve the localization performance.

3. Methods

The overall framework is depicted in Fig. 2. A microscope with camera is used to capture intraocular images. A light fiber with a lens producing a cone-shaped light beam is attached to the surgical instrument.

The projected light pattern is extracted from the camera image. The contour of the projection is extracted, using post-processing and contour detection. Information about the camera setup and the retinal surface is used to reconstruct the three-dimensional shape of the contour. An ellipse is fitted into the contour shape. Based on the fitting result and the geometric properties of the light cone, the source position of the light can be reconstructed.

3.1. Projection pattern reconstruction

First, the camera image is converted from RGB to grayscale. Then, a Gaussian and a median filter are applied to reduce the noise. The result is converted into a binary image using a threshold obtained with the Otsu binarization method [39]. Afterward, the ellipse fitted is used to reconstruct the shape of the spotlight projection. An example for each step is depicted in Fig. 3.

The camera projection of the intraocular surface onto the image plane can be described using the pinhole camera model. Based on the camera model and the surface shape (simplified to be perfectly spherical), we can reconstruct the three-dimensional projection directly from the microscope image. The setting for the reconstruction is depicted in Fig. 4.

Using a point p_c on the camera sensor and the focal point, we can define a line l that intersects the surface of the sphere at the point p_s. By using a cross-section containing p_s, the focal point (F), and the center of the sphere, the problem can be simplified to an intersection between l (yellow in Fig. 4) and a circle. The line l is given by Eq. (1) and the circle by Eq. (2), where f is the focal length, r is the radius of the sphere, and d_0 is the distance between the focal point and the bottom of the sphere. y_1 is the Euclidean distance between the center of the camera sensor and p_c. Here, the coordinate system is defined with the center of the sphere as shown in Fig. 4.

$$y = \frac{f}{y_1}x + (d_0 - r) \tag{1}$$

$$x^2 + y^2 = r^2 \tag{2}$$

The said intersection allows to calculate the distance (d) between the point on the sphere surface p_s represented by p_l and the optical axis.

The resulting Eq. (3) is based on the quadratic formula used to derive the intersection between the line and the circle.

$$d = \frac{\frac{2d_0 f}{y_l} - \frac{2rf}{y_l} + \sqrt{\left(\frac{2rf}{y_l} + \frac{2d_0 f}{y_l}\right)^2 - 4\left(1 + \frac{f^2}{y_l^2}\right)\left(d_0^2 - 2d_0 r\right)}}{2\left(1 + \frac{f^2}{y_l^2}\right)} \tag{3}$$

Knowing the distance (d) between the optical axis and the point p_s, we can obtain the corresponding height (h) using Eq. (4). The height is defined as the distance between p_s and the bottom of the sphere along axis Y, as depicted in Fig. 4.

$$h = r - \sqrt{r^2 - d^2} \tag{4}$$

Given the position $p_c = (x_c, y_c)$ and the distance d, we can calculate the estimated position $p_s = (x_s, y_s, z_s)$, given by Eqs. (5), (6), and (7). Here, s is the physical size of the camera sensor in mm and p is the resolution of the image sensor.

$$x_s = \begin{cases} \frac{d}{\sqrt{1 + \frac{y_c^2}{x_c^2}}}, & \text{if } x_c \geq 0 \\ \frac{-d}{\sqrt{1 + \frac{y_c^2}{x_c^2}}}, & \text{otherwise} \end{cases} \tag{5}$$

$$y_s = \frac{y_p}{x_p} x_s \tag{6}$$

$$z_s = h \tag{7}$$

This allows to fully reconstruct the three-dimensional contour of the intersection based on the shape on the camera sensor.

3.2. Cone-sphere intersection

The intersection between a cone and a sphere is a rather complicated three-dimensional curve that does not lie on a two-dimensional plane. The only exception is the special case, where the center of the sphere lies on the axis of the cone, producing a circle-shaped intersection.

A parametric equation for this curve can be derived using equations defining a sphere and a cone. A right circular cone with the vertex in the origin can be defined using Eq. (8), where β is the opening angle of the spotlight. β is defined as the angle between the axis of the cone and every line from the vertex to a point on its surface. The axis is equal to the Z axis.

$$z^2 = \frac{x^2 + y^2}{\tan(\beta)^2} \tag{8}$$

A sphere can be defined using Eq. (9), where r is the radius of the sphere and (x_0, y_0, z_0) is the position of the center.

$$(x - x_0)^2 + (y - y_0)^2 + (z - z_0)^2 = r^2 \tag{9}$$

To set $y_0 = 0$ and simplify the equation of the intersection, we can rotate the coordinate system around the axis of the cone, so that the center of the sphere is in the plane defined by the Z and X-axis. This does not lead to a loss of generality, as the cone is not affected by the rotation. The resulting equation used for the sphere is given in Eq. (10).

$$(x - x_0)^2 + y^2 + (z - z_0)^2 = r^2 \tag{10}$$

We can then obtain an equation for the intersection by combining Eqs. (8) and (10). The resulting equation is parametric with $x_i = x$ as a parameter. The points $p_i = (x_i, y_i, z_i)$ of the intersection can be calculated with Eqs. (11) and (12), where $c = \tan(\beta)$. The range of values for x is given in Eq. (13) and can be calculated using Eqs. (8) and (9). The definitions for x_1 and x_2 are given in Eqs. (14) and (15).

$$z_i = \frac{z_0 + \sqrt{z_0^2 - \left(1 + c^2\right)\left(x_0^2 - r^2 + z_0^2 - 2x_0 x\right)}}{\left(1 + c^2\right)} \tag{11}$$

$$y_i = \pm\sqrt{z_i^2 c^2 - x^2} \tag{12}$$

$$x = [x_1, x_2] \tag{13}$$

$$x_1 = \frac{\left(x_0 + \frac{z_0}{c}\right) + \sqrt{\left(x_0 + \frac{z_0}{c}\right)^2 - 1 - \frac{1}{c^2}\left(x_0^2 + z_0^2 - r^2\right)}}{1 + \frac{1}{c^2}} \tag{14}$$

$$x_2 = \frac{\left(x_0 - \frac{z_0}{c}\right) - \sqrt{\left(x_0 - \frac{z_0}{c}\right)^2 - 1 - \frac{1}{c^2}\left(x_0^2 + z_0^2 - r^2\right)}}{1 + \frac{1}{c^2}} \tag{15}$$

3.3. Cone-plane intersection

When inspecting the shape of a cone and plane intersection in three dimensions, it is very similar to an ellipse. An example is depicted in Fig. 5(a). This similarity motivates us to simplify the real intersection to the shape of an ellipse, as this can significantly reduce the localization effort. Because instead of trying to reconstruct the location of the light source based on a projection of a three-dimensional curve, we can reconstruct based on the projection of an ellipse. It is known that the intersection between a cone and a plane has the shape of an ellipse, if the angle between the axis of the cone and the plane is higher than the opening angle of the cone. To show the similarity between the cone-sphere intersection to an ellipse, we construct a plane P that intersects the cone and therefore produces an ellipse-shaped intersection.

The cone-plane intersection should be close to the cone-sphere intersection. First, we take the two points $(\mathrm{A}(x_1, 0, z_A)$ and $\mathrm{B}(x_2, 0, z_B))$ on the cone-sphere intersection with the biggest distance between each other and connect them with a line. The resulting plane P is made perpendicular to the XOY plane and contains this line. The x-coordinates of these two points are the ends of the range for the values of x and can be calculated using Eqs. (14) and (15). The Z-coordinates of A and B are calculated using the cone equation as shown in Eq. (16). Figure 5(b) depicts an example for the constructed plane P (blue).

$$z_A = \frac{x_1}{c}, z_B = \frac{-x_2}{c} \tag{16}$$

The resulting plane P is defined by Eq. (17).

$$P: z = \frac{z_A - z_B}{c(z_A + z_B)}x + z_1 - \frac{x_1(z_A - z_B)}{c(z_A + z_B)} \tag{17}$$

This equation can be used in combination with Eq. (8) to obtain the cone-plane intersection points $p_i^{'} = (x_i^{'}, y_i^{'}, z_i^{'})$ as a parametric $(x_i^{'} = x)$ equation. $y_i^{'}$ and $z_i^{'}$ are given by Eqs. (18) and (19). Due to the definition of the plane, the range of values for x is also given by Eq. (13).

$$y_i^{'} = \pm\sqrt{\left(\frac{z_A - z_B}{c(z_A + z_B)}x - z_A - \frac{x_1(z_A - z_B)}{c(z_A + z_B)}\right)^2 c^2 - x^2} \tag{18}$$

$$z_i^{'} = \sqrt{\frac{x^2 + y_i^{'2}}{c^2}} \tag{19}$$

From the definition of the plane P, we know that the intersections have the two points A and B in common. To find the maximum difference between these two intersections, we can use the points $(x_h, 0, z_h)$ where the surfaces intersecting the cone have their biggest difference. z_h and x_h are defined in Eqs. (20) and (21).

$$z_h = \cos\left(\sin^{-1}\left(\cos\left(\beta\right)\frac{x_0}{r}\right)\right)r + z_0 \tag{20}$$

$$x_h = \begin{cases} \sqrt{r^2 - (z_h - z_0)^2} + x_0, & \text{if } x_0 \geq 0 \\ -\sqrt{r^2 - (z_h - z_0)^2} + x_0, & \text{otherwise} \end{cases} \tag{21}$$

This allows us to directly calculate the maximum difference between the two intersections (the real intersection and simplified ellipse) by using the parametric equations. For our use case, we define an area of interest which is shown in Fig. 3. It is a 10 mm × 10 mm × 5 mm range, mainly defined by the microscope view and surgical region. The opening angle β of the cone is independent of the instrument location and depends only on the designed spotlight's lens. Therefore, we can calculate the maximum difference for different values for β. This gives guidance on which angles could be suitable in regard to an error tolerance. The resulting maximum differences are given in Table I.

For our use case, these differences are negligible for the listed opening angles and we can see the projection as an ellipse without introducing a significant error ($\ll 10\ \mu$m).

3.4. Ellipse to cone reconstruction

For the ellipse fitting, the reconstructed shape of the contour is rotated onto the XOY plane as shown in Fig. 6. After reconstructing the vertex of the cone, the inverse rotations are applied. The ellipse can be defined using the position of its center, the length of the major axis a, and minor axis b. The size of the minor axis is related to the distance between the vertex of the cone and the plane. The relationship between a and b depends on the angle between the cone and the XOY plane.

To find the vertex position, a right triangle is used as depicted in Fig. 6. One corner of the triangle is the vertex position, and one corner is in the center position. The side s_2 is perpendicular to the XOY plane, and the side s_1 follows the major axis. The length of the side s_1 and s_2 can be calculated using Eqs. (22), (23), and (24),

$$\alpha = \sin^{-1}\left(\sqrt{1 - \frac{b^2}{a^2}}\cos(\beta)\right) \tag{22}$$

$$s_1 = a\frac{\sin(2\alpha)}{\sin(2\beta)} \tag{23}$$

$$s_2 = a\left(\frac{\cos(2\alpha)}{\sin(2\beta)} + \frac{1}{\tan(2\beta)}\right) \tag{24}$$

where α is the angle between s_2 and the hypotenuse of the triangle SC. As the ellipse lies in the XOY plane. The spotlight position in XYZ is defined as $p_l = (x_l, y_l, z_l)$ shown in Fig. 6. The x_l and y_l can be calculated using the rotation of the ellipse and s_1. z_l equals to the length of s_2. Due to the symmetry of the ellipse, two possible positions for the vertex exist. Knowing the rough position of the insertion point allows us to narrow it down to one position. To derive the final result, the inverse rotations have to be applied to the vertex position.

3.5. Multiple spotlights

As the single spotlight may be prone to errors, we further analyze a setup with multiple spotlights. To evaluate the performance of such a setup, an instrument with three attached spotlights is evaluated. For each projection, the possible vertex positions are reconstructed independently following the algorithm for the single spotlight. To choose the resulting position, all possible combinations including three positions are evaluated based on their spatial difference. The set with the lowest difference is selected. From these three positions, the median position is selected as the final result. The workflow is depicted in Fig. 1(e–g).

4. Experiments and results

The localization algorithm is tested using a simulation. Realistic scenes are rendered with the 3D creation suite Blender 2.8. The algorithm is implemented using Python and the computer vision library OpenCV 3.4. The two versions (single spotlight and three spotlights) are compared by moving the spotlights along two fixed routes.

4.1. Blender scene

The eyeball is modeled using a sphere with a radius of 12 mm. To increase the realism, a retina texture is added. The camera is positioned above the sphere facing downwards. The properties of the camera and the spotlight, as introduced in the previous section, are listed in Table II.

For the version with multiple spotlights, the three spotlights are angled to ensure that their projection does not overlap for the given working range. The applied rotations are given in Table III.

4.2. Evaluation

For the evaluation, the instrument is moved along two given paths, and the localization algorithm is executed 100 times during the movement. The two paths are depicted in Fig. 7. During the movement, the pose of the instrument with the spotlight is constrained by the RCM.

The positioning error is defined as the Euclidean distance between the result of the localization and the real position. Additionally, the error for the rotation of the instrument, split into rotations around the Y_S and Z_S axis in Fig. 4, is given. The results are plotted in Figs. 8 and 9. The average errors (AE) and maximum errors (ME) are listed in Table IV.

The impact of the spotlight appearance is additionally tested by performing the simulations with different light intensities. This provides a sensitivity analysis of the proposed method to the selection of spotlight source power. The results are plotted in Figs. 10 and 11. When increasing the spotlight power to more than 0.25 W, the error performance reduces and keeps steady. An infrared light source and an infrared camera could be used to further enhance the sharpness of the spotlight projection.

To evaluate the impact of small deformations (caused by retinal disease, e.g., macular hole) on the retinal surface, a setup is tested by adding 15 bumps with a diameter of around 0.5 mm and a deviation in height from the sphere surface of 0.1 mm [40]. The bumps are placed in a 3×5 grid formation across the area of interest. The result is shown in Table V with helix trajectory. The AE are very close to the test without the deformation. The maximum positioning error of the version with a single spotlight is significantly higher with a value of 0.210 mm compared to 0.133 mm in the multiple spotlights case. The maximum error of the version with multiple spotlights is equal to the maximum error during the test without the deformations.

5. Conclusion

In this paper, we presented a theoretical analysis of using a spotlight-based instrument localization for retinal surgery. Different from previous work, the projection of the spotlight is directly used to infer the pose of the instrument. The concept is tested using a high-fidelity simulation environment, both with a single and with three spotlights. In the conducted tests, the single spotlight version is able to localize the position of the instrument with an average error of 0.028 mm, while the multiple spotlights version yields 0.024 mm. This shows that the proposed concept works in theory, making the performance boundaries promising for retinal surgery. The main limitation of current work is that the eyeball is treated as a sphere, which however in the realistic the eyeball somehow has a degree of deformation. This need to be further verified in the real scenario. The robustness and reliability of method can be further improved via the online method. Inspired by the work from [41], the future work would be using the artificial network method in the assembly line to learn and optimize for an online estimation which can enhance the robustness and accuracy of the instrument position and pose inside the eye.

Financial support.

The authors would like to acknowledge the Editor-In-Chief, Associate Editor, and anonymous reviewers for their contributions to the improvement of this article. We would like to thank the financial support from the U.S. National Institutes of Health (NIH: grants no. 1R01EB023943-01 and 1R01 EB025883-01A1) and TUM-GS internationalization funding. The work is also supported by the ZJU-100 Young Talent Program.

References

[1]. WHO, Towards Universal Eye Health: A Global Action Plan 2014 to 2019 (WHO, Geneva, 2013).

[2]. Gijbels A, Poorten EV, Gorissen B, Devreker A, Stalmans P and Reynaerts D, "Experimental Validation of a Robotic Comanipulation and Telemanipulation System for Retinal Surgery," In: 2014 5th IEEE RAS EMBS Int. Conf. Biomed. Robot. Biomechatronics (IEEE, 2014) pp. 144–150.

[3]. Wei W, Goldman R, Simaan N, Fine H and Chang S, "Design and Theoretical Evaluation of Micro-Surgical Manipulators for Orbital Manipulation and Intraocular Dexterity," In: Robot. Autom. 2007 IEEE Int. Conf (IEEE, 2007) pp. 3389–3395.

[4]. Taylor R, Jensen P, Whitcomb L, Barnes A, Kumar R, Stoianovici D, Gupta P, Wang Z, Dejuan E and Kavoussi L, "A steady-hand robotic system for microsurgical augmentation," Int. J. Robot. Res 18(12), 1201–1210 (1999).

[5]. Ullrich F, Bergeles C, Pokki J, Ergeneman O, Erni S, Chatzipirpiridis G, Pané S, Framme C and Nelson BJ, "Mobility experiments with microrobots for minimally invasive intraocular Surgery: Microrobot experiments for intraocular surgery," Invest. Ophthalmol. Vis. Sci 54(4), 2853–2863 (2013).

[6]. Rahimy E, Wilson J, Tsao TC, Schwartz S and Hubschman JP, "Robot-assisted intraocular surgery: Development of the IRISS and feasibility studies in an animal model," Eye 27(8), 972–978 (2013).

[7]. Li Z, Xu C, Wei Q, Shi C and Su C-Y, "Human-inspired control of dual-arm exoskeleton robots with force and impedance adaptation," IEEE Trans. Systems Man Cybern. Syst 50(12), 5296–5305 (2018).

[8]. Wu X and Li Z, "Cooperative manipulation of wearable dual-arm exoskeletons using force communication between partners," IEEE Trans. Ind. Electron 67(8), 6629–6638 (2019).

[9]. Li Z, Deng C and Zhao K, "Human-cooperative control of a wearable walking exoskeleton for enhancing climbing stair activities," IEEE Trans. Ind. Electron 67(4), 3086–3095 (2019).

[10]. Carbone G and Ceccarelli M, "A serial-parallel robotic architecture for surgical tasks," Robotica 23(3), 345–354 (2005).

[11]. Wang H, Wang S, Ding J and Luo H, "Suturing and tying knots assisted by a surgical robot system in laryngeal mis," Robotica 28(2), 241–252 (2010).

[12]. Qi W and Aliverti A, "A multimodal wearable system for continuous and real-time breathing pattern monitoring during daily activity," IEEE J. Biomed. Health 24(8), 2199–2207 (2019).

[13]. Qi W and Su H, "A cybertwin based multimodal network for ecg patterns monitoring using deep learning," IEEE Trans. Ind. Inform 18(10), 6663–6670 (2022).

[14]. Qi W, Ovur SE, Li Z, Marzullo A and Song R, "Multi-sensor guided hand gesture recognition for a teleoperated robot using a recurrent neural network," IEEE Robot. Autom. Lett 6(3), 6039–6045 (2021).

[15]. Su H, Qi W, Schmirander Y, Ovur SE, Cai S and Xiong X, "A human activity-aware shared control solution for medical human-robot interaction," Assembly Autom. 42(3), 388–394 (2022).

[16]. Edwards T, Xue K, Meenink H, Beelen M, Naus G, Simunovic M, Latasiewicz M, Farmery A, de Smet M and MacLaren R, "First-in-human study of the safety and viability of intraocular robotic surgery," Nat. Biomed. Eng 2(9), 1–656 (2018).

[17]. Heiserman DL, Build Your Own Working Robot (G/L Tab Books, Blue Ridge Summit, PA, 1976).

[18]. Yurtsever E, Lambert J, Carballo A and Takeda K, "A survey of autonomous driving: Common practices and emerging technologies," IEEE Access 8, 58443–58469 (2020).

[19]. Yang G-Z, Cambias J, Cleary K, Daimler E, Drake J, Dupont PE, Hata N, Kazanzides P, Martel S, Patel RV, Santos VJ and Taylor RH, "Medical robotics-regulatory, ethical, and legal considerations for increasing levels of autonomy," Sci. Robot 2(4), 8638 (2017).

[20]. Lu B, Chu HK, Huang K and Cheng L, "Vision-based surgical suture looping through trajectory planning for wound suturing," IEEE Trans. Autom. Sci. Eng 16(2), 542–556 (2018).

[21]. Li Z, Zhao K, Zhang L, Wu X, Zhang T, Li Q, Li X and Su C-Y, “Human-in-the-loop control of a wearable lower limb exoskeleton for stable dynamic walking,” IEEE/ASME Trans. Mechatron 26(5), 2700–2711 (2020).

[22]. Shi Y, Cai M, Xu W and Wang Y, “Methods to evaluate and measure power of pneumatic system and their applications,” Chin. J. Mech. Eng 32(42), 1–11 (2019).

[23]. Shi Y, Chang J, Wang Y, Zhao X, Zhang Q and Yang L, “Gas leakage detection and pressure difference identification by asymmetric differential pressure method,” Chin. J. Mech. Eng 35(44), 1–9 (2022).

[24]. Zhou M, Yu Q, Huang K, Mahov S, Eslami A, Maier M, Lohmann CP, Navab N, Zapp D, Knoll A and Nasseri MA, “Towards robotic-assisted subretinal injection: A hybrid parallel-serial robot system design and preliminary evaluation,” IEEE Trans. Ind. Electron 67(8), 6617–6628 (2020).

[25]. Zhou M, Wu J, Ebrahimi A, Patel N, He C, Gehlbach P, Taylor RH, Knoll A, Nasseri MA and Iordachita II, “Spotlight-Based 3D Instrument Guidance for Retinal Surgery,” In: 2020 International Symposium on Medical Robotics (ISMR) (May 2020).

[26]. Probst T, Maninis K-K, Chhatkuli A, Ourak M, Poorten EV and Van Gool L, “Automatic tool landmark detection for stereo vision in robot-assisted retinal surgery,” IEEE Robot. Autom. Lett 3(1), 612–619 (2018).

[27]. Yang S, Martel JN, Lobes LA Jr. and Riviere CN, “Techniques for robot-aided intraocular surgery using monocular vision,”Int. J. Robot. Res 37(8), 931–952 (2018).

[28]. Foundation B, Blender [Online] (2020). Available: https://www.blender.org/

[29]. Roodaki H, Grimm M, Navab N and Eslami A, “Real-time scene understanding in ophthalmic anterior segment oct images,” Invest. Ophthalmol. Vis. Sci 60(11), PB095 (2019).

[30]. Zhou M, Roodaki H, Eslami A, Chen G, Huang K, Maier M, Lohmann CP, Knoll A and Nasseri MA, “Needle segmentation in volumetric optical coherence tomography images for ophthalmic microsurgery,” Appl. Sci 7(8), 748 (2017).

[31]. Zhou M, Hamad M, Weiss J, Eslami A, Huang K, Maier M, Lohmann CP, Navab N, Knoll A and Nasseri MA, “Towards robotic eye surgery: Marker-free, online hand-eye calibration using optical coherence tomography images,” IEEE Robot. Autom. Lett 3(4), 3944–3951 (2018).

[32]. Zhou M, Yu Q, Mahov S, Huang K, Eslami A, Maier M, Lohmann CP, Navab N, Zapp D, Knoll A and Ali Nasseri M, “Towards robotic-assisted subretinal injection: A hybrid parallel-serial robot system design and preliminary evaluation,” IEEE Trans. Ind. Electron 67(8), 6617–6628 (2019).

[33]. Weiss J, Rieke N, Nasseri MA, Maier M, Eslami A and Navab N, “Fast 5dof needle tracking in iOCT,” Int. J. Comput. Assist. Radiol. Surg 13(6), 787–796 (2018).

[34]. Seider MI, Carrasco-Zevallos OM, Gunther R, Viehland C, Keller B, Shen L, Hahn P, Mahmoud TH, Dandridge A, Izatt JA and Toth CA, “Real-time volumetric imaging of vitreoretinal surgery with a prototype microscope-integrated swept-source oct device,” Ophthalmol. Retina 2(5), 401–410 (2018).

[35]. Chen Q, Wu H and Wada T, “Camera Calibration with Two Arbitrary Coplanar Circles,” In: European Conference on Computer Vision (Springer, Berlin/Heidelberg, 2004) pp. 521–532.

[36]. Noo F, Clackdoyle R, Mennessier C, White TA and Roney TJ, “Analytic method based on identification of ellipse parameters for scanner calibration in cone-beam tomography,” Phys. Med. Biol 45(11), 3489–3508 (2000).

[37]. Swirski L and Dodgson N, “A Fully-Automatic, Temporal Approach to Single Camera, Glint-Free 3D Eye Model Fitting,” In: Proc. PETMEI (2013) pp. 1–11.

[38]. Yang S, MacLachlan RA, Martel JN, Lobes LA and Riviere CN, “Comparative evaluation of handheld robot-aided intraocular laser surgery,” IEEE Trans. Robot 32(1), 246–251 (2016).

[39]. Otsu N, “A threshold selection method from gray-level histograms,” IEEE Trans. Syst. Man Cybern 9(1), 344–349 (1979).

[40]. Shin J, Chu Y, Hong Y, Kwon O and Byeon S, “Determination of macular hole size in relation to individual variabilities of fovea morphology,” Eye 29(8), 1051–1059 (2015).

[41]. Su H, Hu Y, Karimi HR, Knoll A, Ferrigno G and De Momi E, “Improved recurrent neural network-based manipulator control with remote center of motion constraints: Experimental results,” Neural Netw. 131, 291–299 (2020).

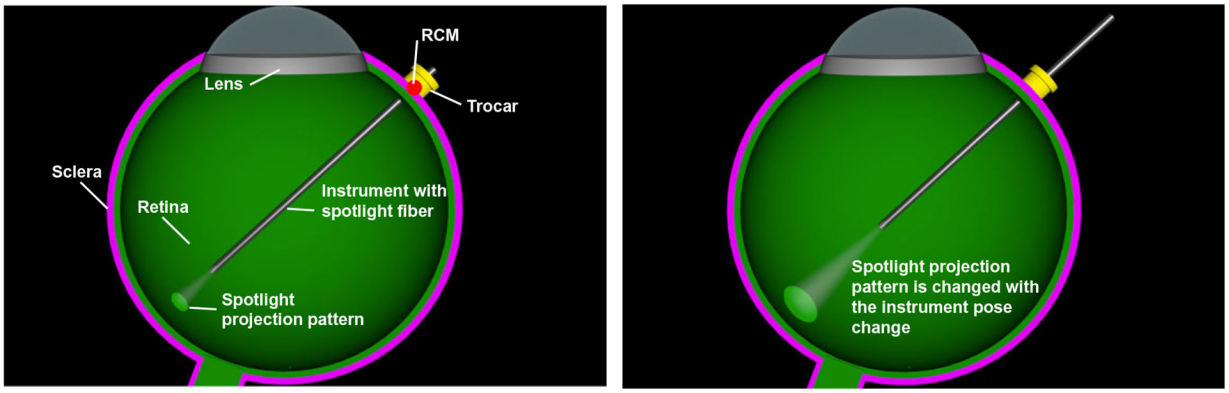

Figure 1.

(a) The simulation setup in Blender. The movement of the instrument is constrained by the remote center of motion (RCM) to reduce the trauma of the incision point on the sclera. (b) The spotlight pattern changes with the location of the instrument.

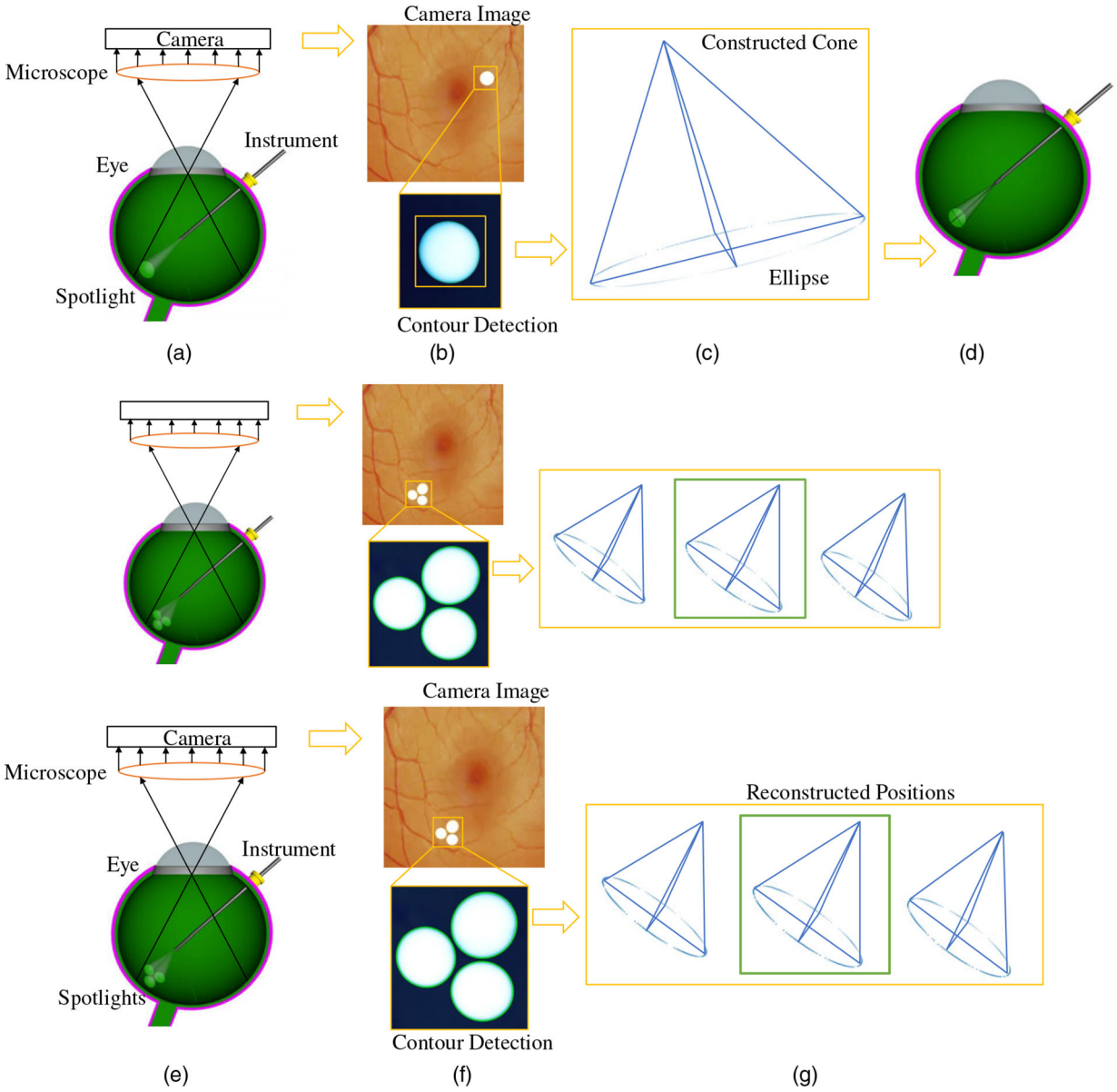

Figure 2.

(a) A spotlight is attached to the instrument. The camera and microscope system are set up to record the projection of the spotlight on the intraocular surface of the eye. (b) Post-processing is used to detect the contour of the projection on the captured images. (c) The known surface is used to reconstruct the real projection. An ellipse is fitted and used to reconstruct the cone. (d) The light cone is placed above the real projection to determine the position of the instrument. (e) For the multiple spotlights scenario, three spotlights are attached to the instrument. (f) The three projections are used independently to reconstruct possible vertex positions. (g) The median position is picked as the result.

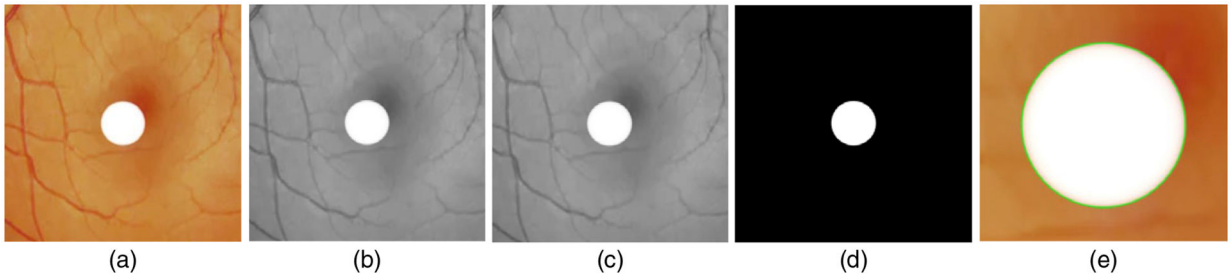

Figure 3.

The original image (a) is converted to a grayscale image (b). A Gaussian and median filter (c) are used reduce noise. The result is converted into a binary image (d) that is used for the contour detection. A closeup of the detected contour (green) on top of the original image can be seen in (e).

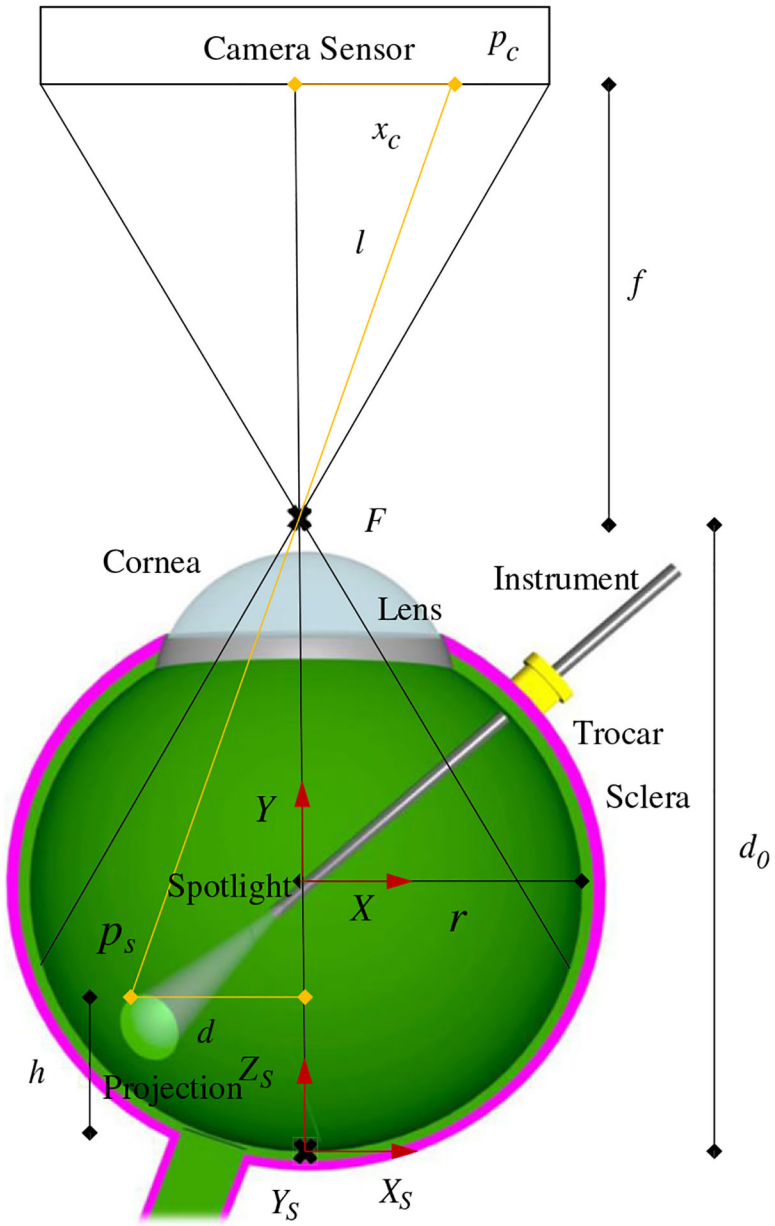

Figure 4.
Cross-section along the optical axis. Used for the reconstruction of the projection.

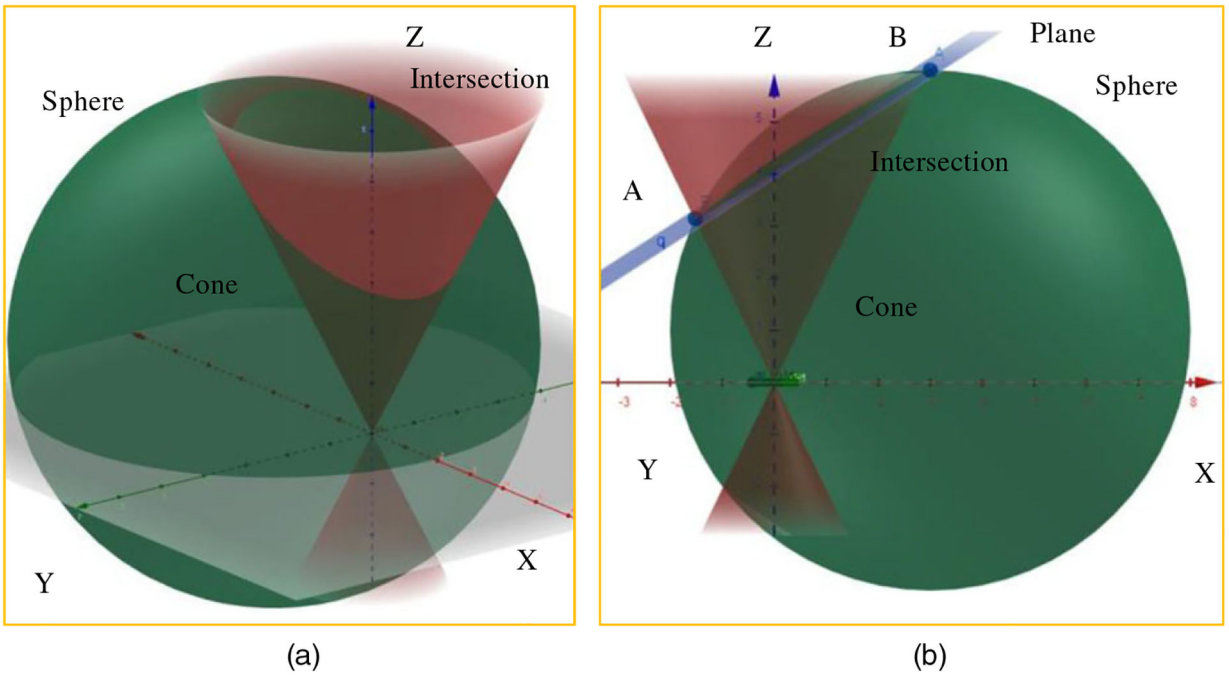

Figure 5.
(a) Intersection between a sphere and a cone. (b) The blue plane is used to show the similarity between the cone-sphere intersection and an ellipse.

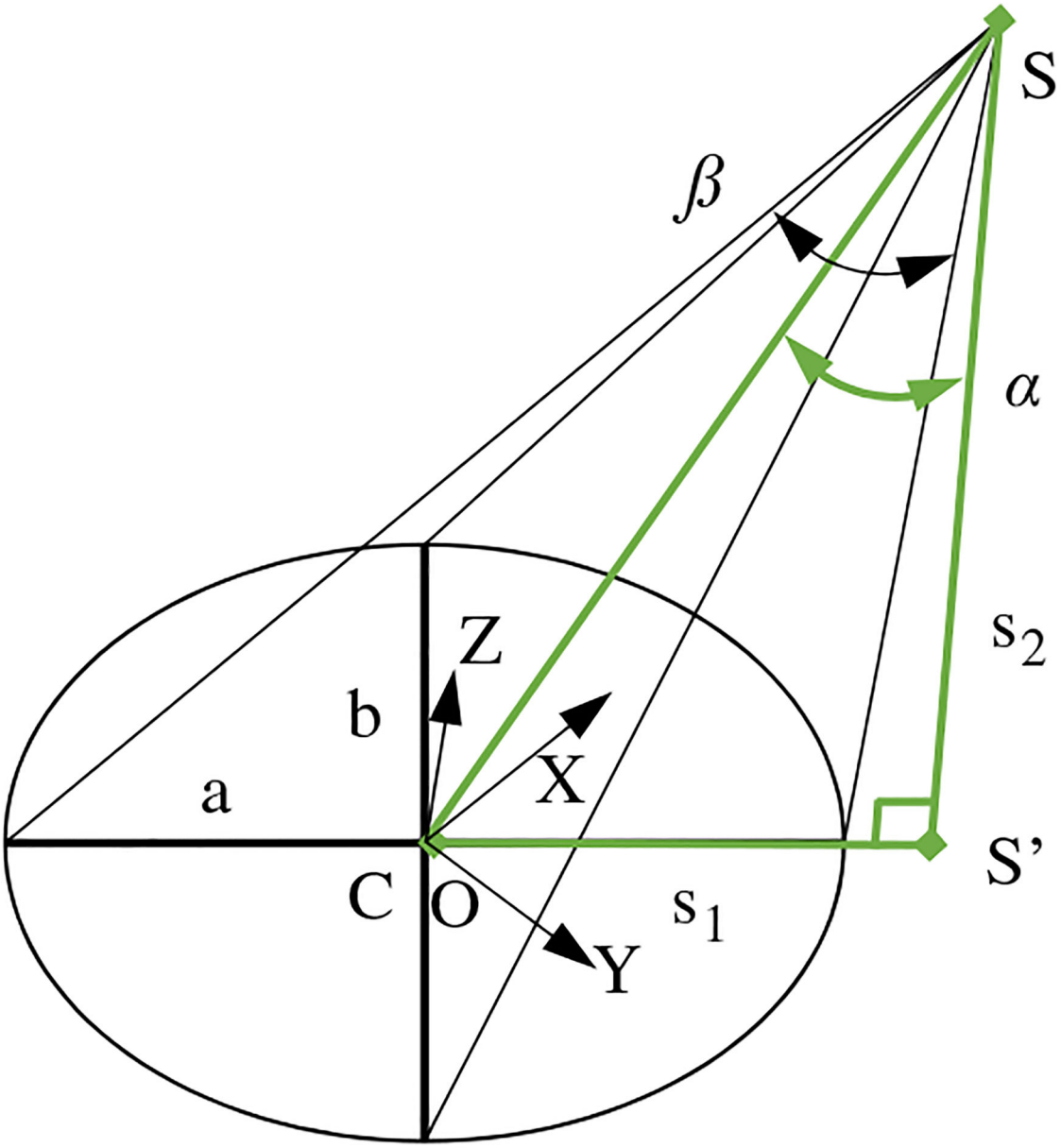

Figure 6.

Triangle (green) used to derive the vertex position based on a given ellipse. *S* denotes the spotlight source. *C* denotes center of ellipse. s_1 is the distance between S' and C. s_2 is the height of the spotlight source *S* with the XOY plane.

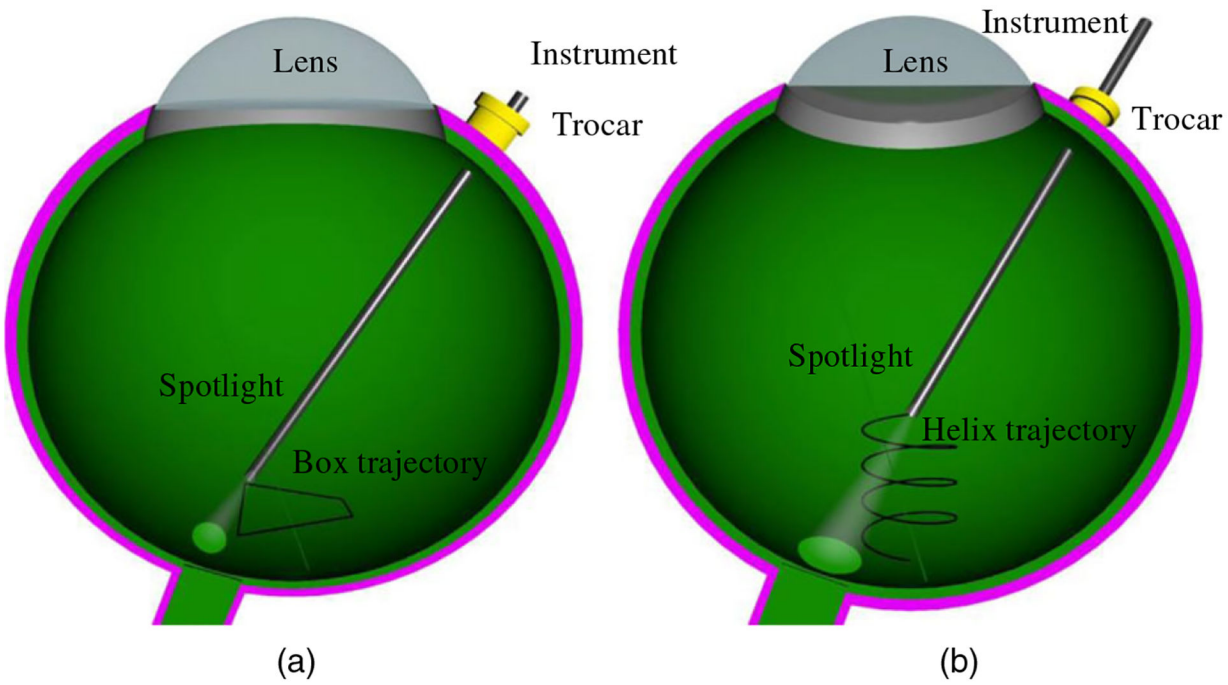

Figure 7.
(a) Path of the spotlight used during the first test (Box). (b) Path of the spotlight used during the second test (Helix).

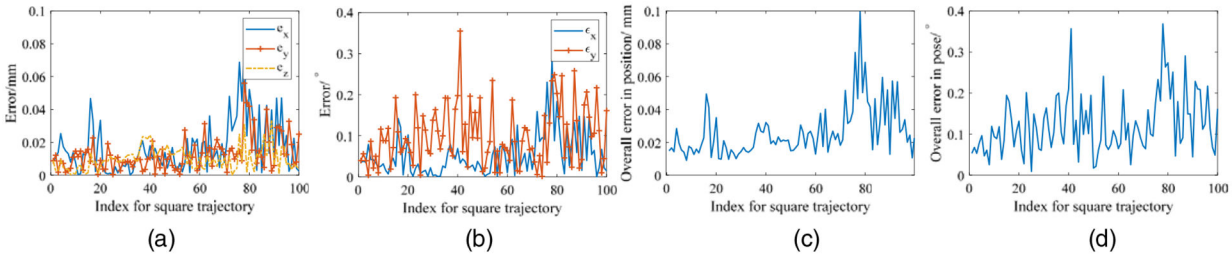

Figure 8.

The error performance with the box trajectory for a single spotlight. e_x, e_y, and e_z denote the error in X_S, Y_S, and Z_S axis shown in Fig. 4, respectively. ϵ_x and ϵ_y denote the rotation error in Y_S and Z_S axis. (a) Positioning error in each direction X_S, Y_S, and Z_S. (b) Orientation error in Y_S and Z_S. (c) Overall error in position. (d) Overall error of orientation.

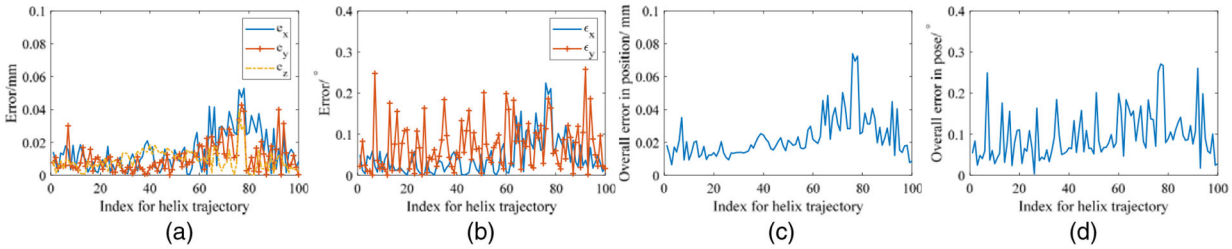

Figure 9.

The error performance with the box trajectory for multiple spotlights. (a) Positioning error in each direction X_S, Y_S, and Z_S. (b) Orientation error in Y_S and Z_S. (c) Overall error in position. (d) Overall error of orientation.

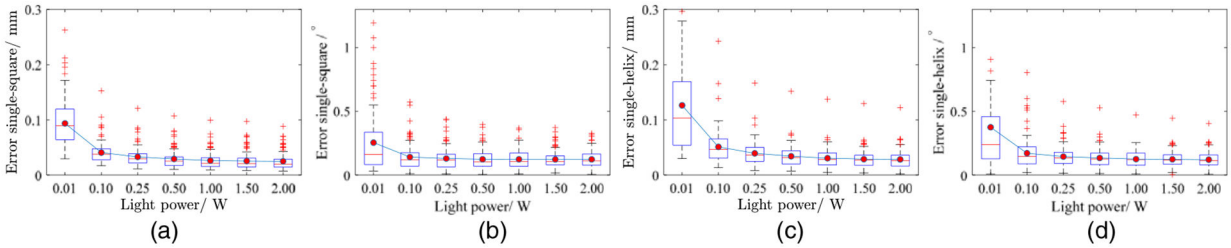

Figure 10.

The error performance with different light intensities. The whiskers show the minimum and maximum recorded distance changes. The start and end of the boxes denote the first and third quartile. The band, red dot, and cross represent the median, mean, and outliers of the recorded changes, respectively. (a) Positioning error with the square trajectory for a single spotlight. (b) Rotation error with the square trajectory for a single spotlight. (a) Positioning error with the helix trajectory for a single spotlight. (d) Rotation error with the helix trajectory for a single spotlight.

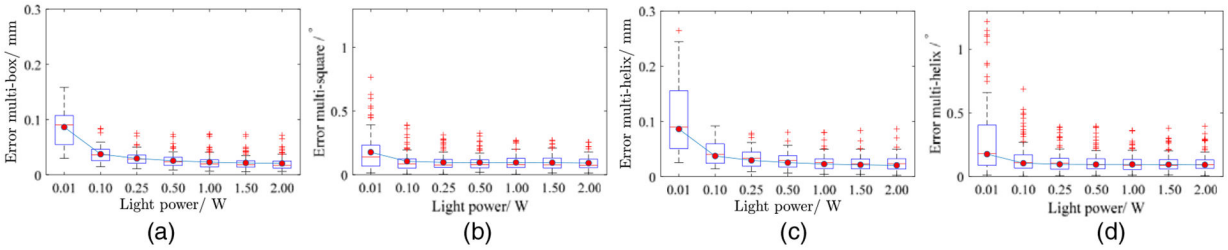

Figure 11.

The error performance with different light intensities. (a) Positioning error with the square trajectory for multiple spotlights. (b) Rotation error with the square trajectory for multiple spotlights. (a) Positioning error with the helix trajectory for multiple spotlights. (d) Rotation error with helix trajectory for multiple spotlights.

Table I.

The maximum difference between the intersections.

β [°]	5	7	9	11	13	15
Difference [μm]	0.08	0.23	0.49	0.91	1.51	2.34

Table II.

Properties of the camera in the Blender simulation.

Resolution (*p*)	**Sensor size (*s*)**	**Focal length (*f*)**	**Angle (*β*)**
5000 pixels	3.6cm	30 cm	9°

Table III.

Rotations applied to each spotlight to achieve the correct angles.

	Spotlight 1	Spotlight 2	Spotlight 3
x	−10°	0°	9°
y	−6°	11°	—6°
Z	0°	0°	0°

Table IV.

Error for different tests.

Error	Position [mm]		Angle [°]	
Spotlight	**Single**	**Three**	**Single**	**Three**
AE (Box)	0.026	0.023	0.123	0.096
AE (Helix)	0.031	0.026	0.125	0.106
ME (Box)	0.100	0.074	0.368	0.271
ME (Helix)	0.137	0.080	0.473	0.362

Table V.

Overall error for the deformed surface with helix trajectory.

Error	Single spotlight	Three spotlights
AE [mm]	0.035	0.027
ME [mm]	0.210	0.080
AE [°]	0.141	0.104
ME [°]	0.996	0.447